

University of Windsor

Scholarship at UWindor

Electronic Theses and Dissertations

Theses, Dissertations, and Major Papers

1-1-1970

Backscattering of light atomic projectiles from thin gold films in the energy range 50-110 keV.

Everett Brimmer
University of Windsor

Follow this and additional works at: <https://scholar.uwindsor.ca/etd>

Recommended Citation

Brimmer, Everett, "Backscattering of light atomic projectiles from thin gold films in the energy range 50-110 keV." (1970). *Electronic Theses and Dissertations*. 6847.
<https://scholar.uwindsor.ca/etd/6847>

This online database contains the full-text of PhD dissertations and Masters' theses of University of Windsor students from 1954 forward. These documents are made available for personal study and research purposes only, in accordance with the Canadian Copyright Act and the Creative Commons license—CC BY-NC-ND (Attribution, Non-Commercial, No Derivative Works). Under this license, works must always be attributed to the copyright holder (original author), cannot be used for any commercial purposes, and may not be altered. Any other use would require the permission of the copyright holder. Students may inquire about withdrawing their dissertation and/or thesis from this database. For additional inquiries, please contact the repository administrator via email (scholarship@uwindsor.ca) or by telephone at 519-253-3000ext. 3208.

**BACKSCATTERING OF LIGHT ATOMIC PROJECTILES FROM THIN Au FILMS
IN THE ENERGY RANGE 50-110 keV**

by

Everett Brimmer

A Thesis

**Submitted to the Faculty of Graduate Studies through the Department
of Physics in Partial Fulfillment of the Requirements for
the Degree of Master of Science at the
University of Windsor**

Windsor, Ontario

1970

UMI Number: EC52789

INFORMATION TO USERS

The quality of this reproduction is dependent upon the quality of the copy submitted. Broken or indistinct print, colored or poor quality illustrations and photographs, print bleed-through, substandard margins, and improper alignment can adversely affect reproduction.

In the unlikely event that the author did not send a complete manuscript and there are missing pages, these will be noted. Also, if unauthorized copyright material had to be removed, a note will indicate the deletion.

UMI[®]

UMI Microform EC52789

Copyright 2008 by ProQuest LLC.

All rights reserved. This microform edition is protected against unauthorized copying under Title 17, United States Code.

ProQuest LLC
789 E. Eisenhower Parkway
PO Box 1346
Ann Arbor, MI 48106-1346

APPROVED BY:

NE Hedgcock
at J. H. Singer
Ch. van Wijk

296563

ABSTRACT

Thin gold films, vacuum deposited onto a beryllium substrate, have been irradiated with $^1\text{H}^+$, $^4\text{He}^+$, $^7\text{Li}^+$, and $^{11}\text{B}^+$ projectiles in the energy range 50-110 keV. The backscatter intensity at a laboratory scattering angle of 136.4 degrees was measured. The intensity is not exactly proportional to film thickness but increases more rapidly. This effect has been attributed to multiple small-angle collisions. Using estimates for the angular divergence of an ion beam as it traverses a thin film, the backscatter intensity has been corrected for compound scattering. The observed scattering cross sections are in good agreement with theory for scattering in a shell-shielded Coulomb potential.

ACKNOWLEDGEMENTS

I wish to thank Dr. A. van Wijngaarden for his supervision throughout the course of this work. I should also like to thank Dr. W. Baylis for suggesting the shell-shielded Coulomb potential, and Mr. B. Miremadi for his valuable assistance during the measurements.

Acknowledgements are also due to Dr. J. P. Marton who measured the thicknesses of the thin gold films.

I am also indebted to the National Research Council of Canada for its financial support in the form of a Graduate Scholarship.

Finally, I am grateful to my wife for her understanding and encouragement.

TABLE OF CONTENTS

ABSTRACT	i
ACKNOWLEDGEMENTS	ii
LIST OF FIGURES	iv
CHAPTER I - INTRODUCTION	1
CHAPTER II - THEORY	3
CHAPTER III - EXPERIMENTAL	10
3:1 Detector Efficiency	10
3:2 Film Thickness	12
CHAPTER IV - RESULTS	14
4:1 Backscatter of ^1H	14
4:2 Backscatter of ^4He , ^7Li and ^{11}B	16
CHAPTER V - ENERGY LOSS IN THE FILM	20
CHAPTER VI - MULTIPLE SCATTERING EFFECTS	25
6:1 Angular Divergence	26
6:2 Correction Factor	27
6:3 Dependence of Backscatter Yield on Film Thickness	30
CHAPTER VII - DISCUSSION	33
APPENDIX I - THE SHELL-SHIELDED COULOMB POTENTIAL	34
APPENDIX II - THE CLASSICAL CROSS SECTION FOR THE SHELL-SHIELDED COULOMB POTENTIAL	36
APPENDIX III - TRANSFORMATION FORMULAE BETWEEN LAB AND CM FRAMES	40
III:1 Relationship of the Cross Sections	43
APPENDIX IV - EXPERIMENTAL DIFFERENTIAL SCATTERING CROSS SECTION	44
BIBLIOGRAPHY	45
VITA AUCTORIS	46

LIST OF FIGURES

1.	Various Potentials as a Function of Internuclear Distance R	7
2.	The Energy Dependence of Various Laboratory Cross Sections for Scattering Through 136.4 Degrees of Various Projectiles From Gold	9, 33a
3.	Schematic Diagram of the Apparatus	11
4.	Energy Dependence of the Observed Backscatter Yield of ^1H From Various Thin Gold Films	15
5.	Energy Dependence of the Observed Backscatter Yield of ^4He From Various Thin Gold Films	17
6.	Energy Dependence of the Observed Backscatter Yield of ^7Li From Various Thin Gold Films	18
7.	Energy Dependence of the Observed Backscatter Yield of ^{11}B From Various Thin Gold Films	19
8.	The Nuclear Stopping Power $(d\epsilon/d\varphi)_n$ as a Function of $\epsilon^{1/2}$ (from Lindhard et al. 1963)	22
9.	Correction Factor for Multiple Scattering as a Function of ϕ_{rms} Evaluated at Half the Film Thickness	29
10.	Observed and Corrected Backscatter Yield as a Function of Film Thickness	31
11.	Asymptotic Views of an Elastic Collision in the Lab System	40
12.	Asymptotic Views of an Elastic Collision in the CM System	41
13.	A Vector Addition Diagram of the Velocities of Particles in the CM and Lab Frames	42

CHAPTER 1

INTRODUCTION

The energy loss of atomic projectiles in solids can be attributed to two separate processes: nuclear recoil and electronic excitation. In a nuclear collision the target nucleus together with its orbital electrons recoils, and the projectile is deflected. In general slow ions lose energy primarily to target atoms and their trajectory consists of a devious path, while fast ions dissipate energy mainly through electronic excitation and travel, therefore, in nearly straight lines. Although the major energy loss mechanism for light atomic projectiles above about 10^4 eV is the electronic one, some nuclear collisions occur and backscattering of incident ions can result. At energies above 10^6 - 10^7 eV, such interactions are almost purely Coulombic for the lightest atomic projectiles, and the scattering, therefore, exhibits Rutherford behaviour. At lower energies the incident particle at its point of maximum potential energy in the collision sees a weakened Coulomb potential, due to electronic screening between the two nuclei. One of the aims of this investigation is to study the interaction potential for nearly head-on collisions of light atomic projectiles with gold. In such collisions the incident ions can be scattered back through the surface of the target sample into the surrounding vacuum.

Backscattering of light atomic projectiles is used to investigate the location of impurity atoms in crystals (Mayer et al. 1968), and to explain sputtering (Behrisch 1969; Sigmund 1968 and 1969; van Wijngaarden et al. 1970). McCracken and Freeman (1969) have studied

the energy distribution of hydrogen ions backscattered from thick heavy targets. They assumed a model for the process in which "the incident ion slows down in the target material without undergoing any scattering, that it is then scattered [in a pure Coulomb potential] through a large angle and that it returns to the surface without further scattering." The energy dependence of their observed backscatter intensity agrees fairly well with predictions based on their model, but the intensity is high by a factor of about 4. A normalization by 3.1 is required to fit Behrisch's angular distribution of H^+ backscattered from copper. They therefore concluded that a single-collision model was inadequate. To determine the significance of multiple small-angle collisions in this work, an analysis of the dependence of backscatter yield on target thickness has been made.

CHAPTER 11

THEORY

Consider an ion beam incident on a target film of several atomic layers thickness. If the ion mass m_1 is less than the target atom mass m_2 , single-collision backscattering can occur. In such a violent collision only the target atom and the projectile need be considered. This is so because the target atom is nearly free (Bergström and Domeij 1966) since bond energy of neighbouring atoms is small for keV projectiles. The projectile does not see the target atom's neighbours since the transit time across the interaction region of the target atom (typically about 10^{-16} sec) is much shorter than normal vibrational periods (10^{-13} - 10^{-14} sec) in the solid. Multiple scattering results whenever the projectile sufficiently penetrates the electron clouds of more than one atom, and occurs therefore in all thick target media. The two-body scattering problem, however, must be understood before we can proceed to study multiple scattering effects.

The scattering of keV projectiles from atoms is not strictly elastic, since electronic excitation of both the incident ion and the target atom usually results. The energy loss to electrons, however, is a small fraction of the incident ion energy and the single scattering event can be considered elastic.

Because of electronic screening, the actual potential energy of two interacting atoms is unknown. At high energies, when the colliding nuclei interpenetrate each other's electron clouds, electronic screening is small and the potential energy is almost purely Coulombic:

$$V(R) = Z_1 Z_2 e^2 / R \quad (1)$$

The scattering is described by the familiar Rutherford cross section

$$(d\sigma/d\Omega)_R = (b/4)^2 \csc^4(\theta/2) \quad (2)$$

where b is the collision diameter, the distance of closest approach of two unscreened nuclei in a head-on collision:

$$b = Z_1 Z_2 e^2 / (\frac{1}{2}uv^2). \quad (3)$$

Here u is the reduced mass of the projectile-target system, and v is their initial relative velocity. The Rutherford cross section is accurate only as long as the minimum distance of approach $\frac{1}{2} b (1 + \csc \theta/2)$ is much less than the effective screening radius of the interacting particles.

For ^1H backscattered from Au at $\theta_L = 136.4^\circ$, for example, we find deviations from Rutherford behaviour at energies as high as 100 keV.

For more massive projectiles and or smaller scattering angles, the lower energy bound for Rutherford behaviour increases.

Several interatomic potentials have been proposed to allow for the electronic screening of the nuclear Coulomb field. Bohr (1948) suggested that the interaction between two atomic structures is given by the screened Coulomb potential energy

$$V(R) = (Z_1 Z_2 e^2 / R) \exp(-R/a_s). \quad (4)$$

* All Center-of-Mass (CM) quantities will be written without a subscript. Laboratory (lab) quantities will be denoted by the subscript l .

The range of the screening, and hence a measure of the overall size of the two interacting particles, is given by the Bohr screening length

$$a = a_0 / \sqrt{Z_1^{2/3} + Z_2^{2/3}} \quad (5)$$

Here $a_0 = 0.529 \text{ \AA}$, the Bohr radius. Firsov (1958) employs a screening factor calculated from the Thomas-Fermi statistical model of the atom

$$a = 0.8853 a_B. \quad (6)$$

We shall refer to and use this latter value exclusively as the screening parameter in the remainder of this thesis.

For $R \ll a$, the Bohr potential energy is approximately given as

$$V(R) = (Z_1 Z_2 e^2 / R) (1 - R/a) H(1 - R/a) \quad (7)$$

where $H(x)$ is the Heaviside step function

$$H(x) = \begin{cases} 1 & \text{if } x > 0 \\ 0 & \text{if } x < 0. \end{cases}$$

Eq. 7 represents the interaction energy between a charge $Z_1 e$ and a charge $Z_2 e$ when the latter is surrounded by a spherical shell of negative charge density

$$-Z_2 e (4\pi a^2)^{-1} \delta(R - a) \quad (\text{See Appendix 1}).$$

An important advantage of the shell-shielded potential is that the corresponding cross section has a simple analytic form:

$$\frac{d\sigma}{d\Omega} = \left[\frac{ab(a + b/2)}{4a(a + b) \sin^2(\theta/2) + b^2} \right]^2 = k \left(\frac{d\sigma}{d\Omega} \right)_R \quad (8)$$

where the correction factor k is

$$k = \left[\frac{1 + \frac{1}{2}b/a}{1 + b/a + b^2/(4a^2 \sin^2 \frac{1}{2}\theta)} \right]^2 \quad (9)$$

(See Appendix 11).

Eq. 8 is readily integrated to give the classically expected finite total cross section

$$\sigma = \int_{4\pi} d\Omega \frac{d\sigma}{d\Omega} = a^2 \pi \quad (10)$$

In the limit of high incident energy (small b) and large screening radius, b/a is small, and $\left(\frac{d\sigma}{d\Omega}\right)$ (Eq. 8) approaches $\left(\frac{d\sigma}{d\Omega}\right)_R$ (Eq. 2).

Smith et al. (1967) have used variational methods to obtain the best empirical fit of the functional form

$$V(R) = Ae^2/R \exp(-R/C) \quad (11)$$

to experimental data for scattering of He on Ne and Ar in the energy range of 10 eV to 100 keV. In Eq. 11 the variational parameters are A and C . The empirical values for C are about twice as large as the corresponding Thomas-Fermi screening parameters (Eq. 6). Furthermore Abrahamson (1963) has calculated Thomas-Fermi-Dirac potentials for the interaction of noble-gas atoms, and has found good agreement with experiment at small R . In Figure 1 Abrahamson's results for Ne-Ne, Kr-Kr, and Rn-Rn interactions are shown, along with the analytic potentials of Eqs. 1, 4 and 7, for both screening lengths a and $2a$. Curve number 3, representing the shell-shielded Coulomb potential energy

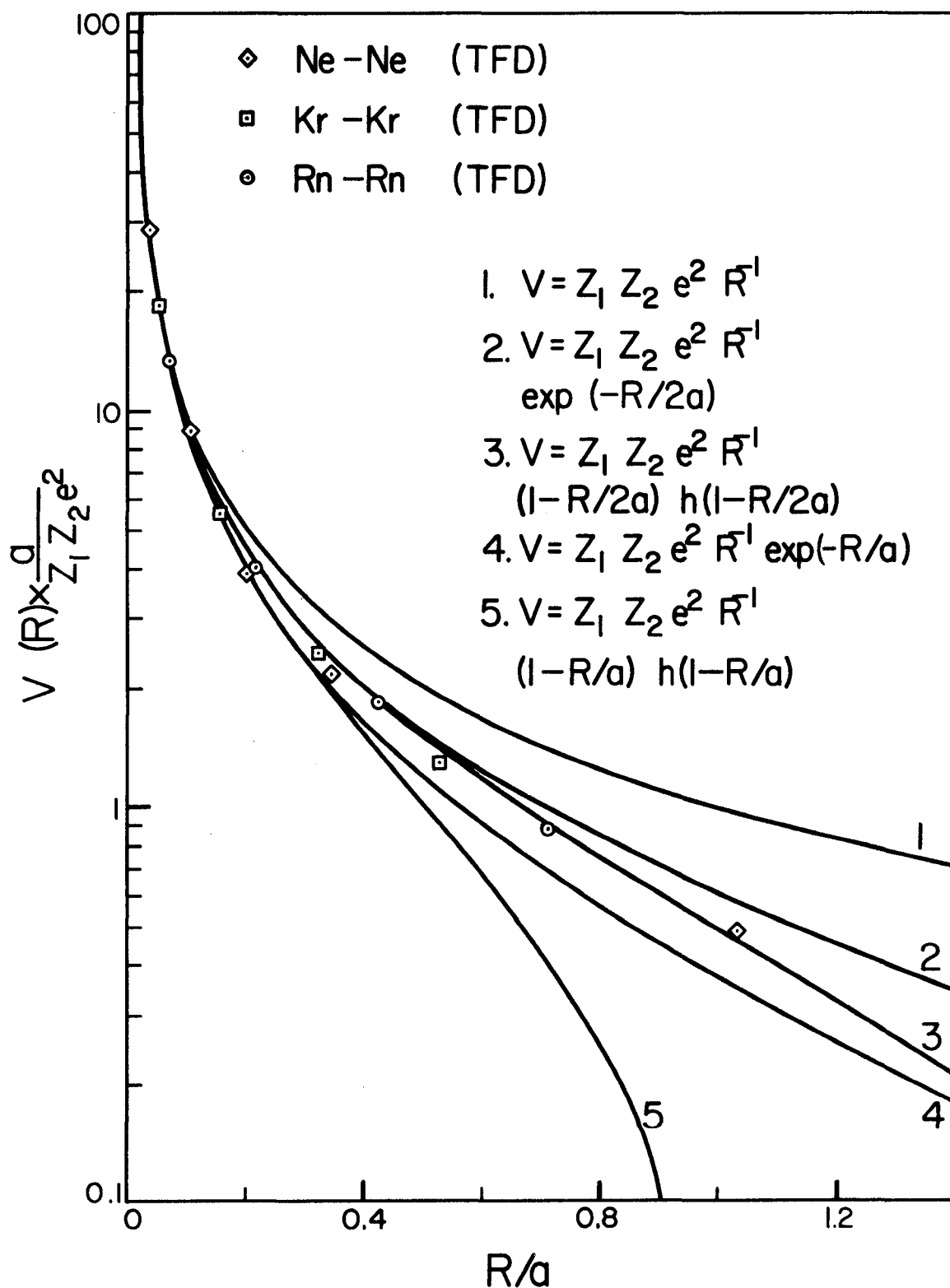


Figure 1. Various potentials as a function of internuclear distance R . The points are Abrahamson's (1963) calculations for interactions between like noble-gas atoms in the Thomas-Fermi-Dirac theory.

$$V(R) = (Z_1 Z_2 e^2 / R) (1 - R/2a) H(1 - R/2a) \quad (12)$$

gives the best fit for $R \lesssim a$. The corresponding cross section is given by Eqs. 8 and 9 with a replaced by $2a$.

Cross sections for Bohr's screened potential have been calculated numerically for several values of b/a (Everhart et al. 1955). For $\pi/2 \lesssim \theta < \pi$ and $b/a \lesssim 1$, the Rutherford cross section is as much as a factor of 2.5 larger than Everhart's values, whereas the shell-shielded cross section (Eq. 8) always lies within 10% of the numerical results.

Our experimental scattering cross sections (to be discussed below) for ^1H , ^4He , ^7Li and ^{11}B on Au for a fixed laboratory scattering angle of 136.4° and at laboratory energies from 50 to 110 keV are presented as circles in Fig. 2. The Rutherford cross sections (dash-dot lines) lie well above the shell-shielded (dashed lines) and Everhart's exponentially-screened Coulomb values (\diamond 's). The good agreement between the shell-shielded and exponentially-screened Coulomb cross sections is evidence that backscattering is governed primarily by the potential at distances $R < a$. This is so because the former interaction is zero for $R > a$ while the latter is not. The solid curve, presenting the cross sections of the shell-shielded Coulomb potential with the screening radius doubled, agrees fairly well with the reduced experimental data (Chapters V and VI) both in energy dependence and absolute value.

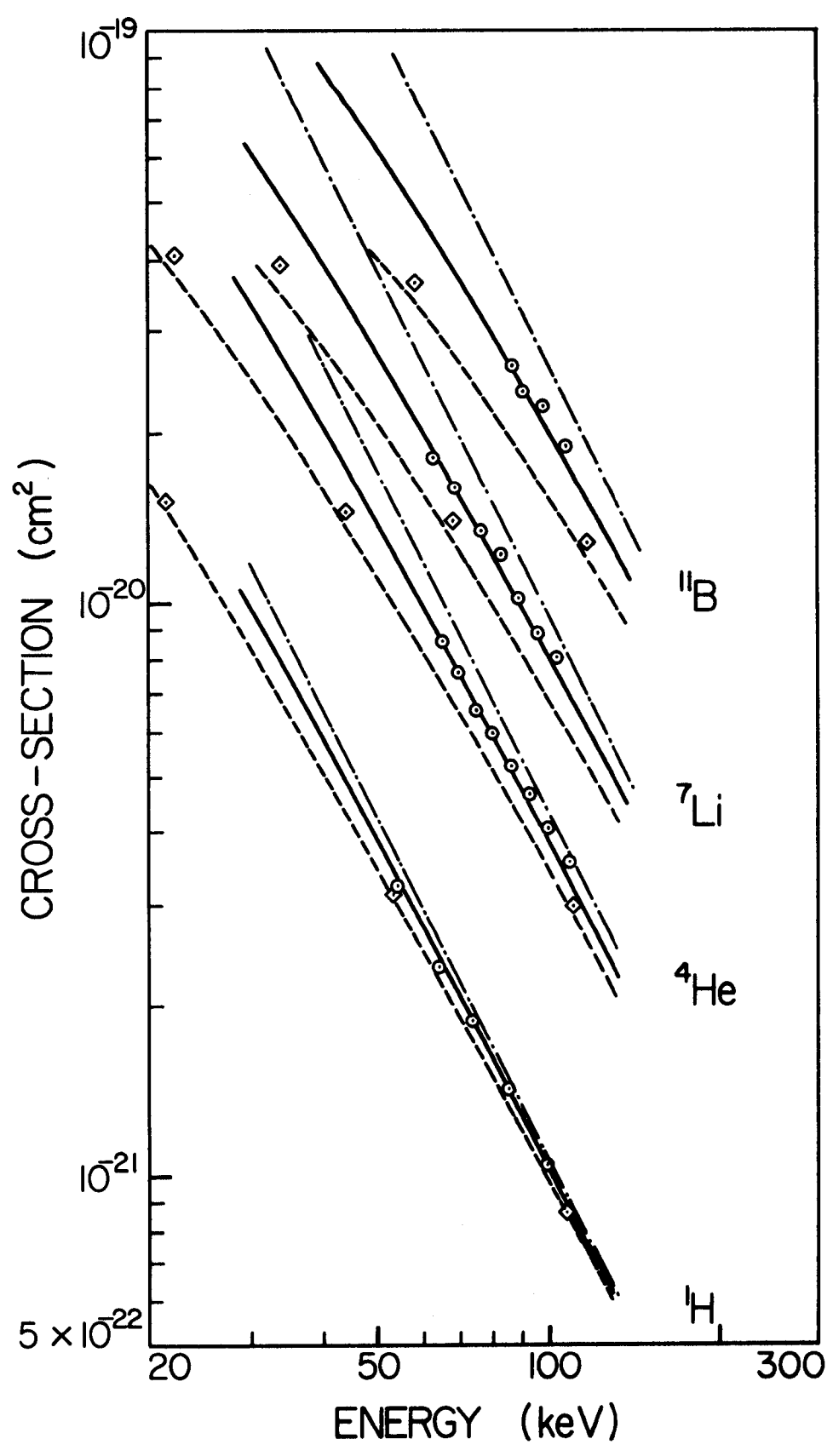


Figure 2. Energy dependence of lab cross sections at $\theta_L=136.4^\circ$ for various projectiles on gold. -·-· Rutherford; — shell-shielded Coulomb $a \rightarrow 2a$; ---- shell-shielded Coulomb; \diamond screened Coulomb; \circ experimental.

CHAPTER 111

EXPERIMENTAL

Figure 3 is a schematic diagram of the apparatus. Monoenergetic ion beams at energies below 120 keV are obtained from a magnetic analyzer (van Wijngaarden et al. 1970). The angular divergence of the emerging beam is limited to within 0.2° by a circular slit system. After collimation the ion beam enters the target chamber which is maintained at a pressure of the order of 10^{-7} Torr. Regularly spaced thin target films of Au, vacuum deposited onto a thick Be plate, can be moved across the path of the ion beam as indicated by the arrows. A Faraday cup connected to a bellows can be moved into the path of the ion beam. The absolute value of the current is measured to within 2% by a Keithley 410 electrometer. An Ortec Model E-013-025-100 surface barrier detector, subtending a solid angle $\Delta\Omega = (5.25 \pm 0.03) \times 10^{-4}$ sr, is positioned at 136.4° with respect to the incident ion beam. The pulses from the detector are fed through a preamplifier (Ortec Model 109a), a main amplifier (Ortec Model 485), a single channel analyzer (Ortec Model 406a), and are recorded by a digital ratemeter (Ortec Model 434).

3:1 Detector Efficiency

Any ion which is detected has passed through the Au electrode (228 Å thickness) of the surface barrier detector, and then produced sufficient ionization to create a pulse discernible above the noise of the detector. To find the minimum energy for 100% detection, the detector was placed directly in the path of monoenergetic $^1\text{H}^+$ and $^4\text{He}^+$ beams. With the lower discriminator level of the single channel analyzer

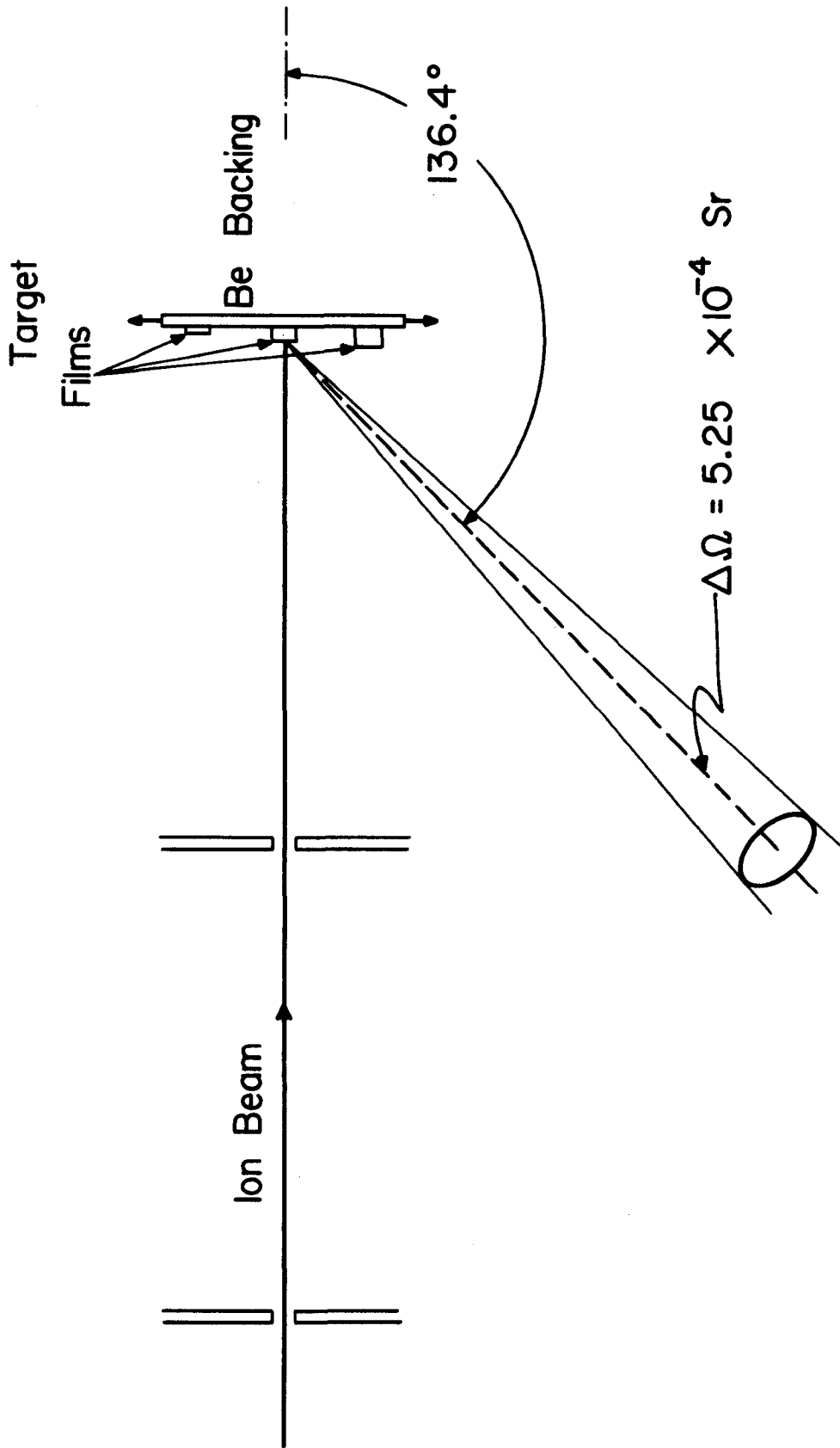


Figure 3. Schematic diagram of the apparatus.

fixed just above the detector noise level, the detector efficiency (number of counts per incident projectile) was observed to be essentially perfect for protons at primary energies $E \gtrsim 40$ keV and for ${}^4\text{He}$ at $E \gtrsim 50$ keV. As the primary energy decreased below these values, so did the efficiency of the detector. Below 10 keV no particles could be detected.

It is the counting efficiency for the backscattered projectiles which is of interest in the present experiment. The energy loss for these projectiles in the thin target films is quite small (Chapter V), and 100% backscattered-projectile counting efficiency was expected for primary energies down to about the same limits. To verify this, only incident energies were used for each projectile and each film for which the counting rate of the backscattered ions into the detector ($\theta_L = 136.4^\circ$) remained constant for a small range of the lower discriminator settings.

3:2 Film Thickness

Five thin Au films were vacuum deposited simultaneously onto Be and glass substrates using an Edwards Coating Unit (Model 12EA/722). The thicknesses of the Au films on the glass substrate were measured using optical techniques (Marton and Schlesinger 1969). To check that corresponding Au films on the two substrates were of equal thickness, the following experiment was performed. The glass-backed and Be-backed Au films were successively irradiated with ${}^4\text{He}$ projectiles and the intensities of the backscattered projectiles from the various thin films and the two substrates were measured. The backscatter yield (number of backscatter counts per incident projectile) from the Be substrate was 0.2% of that from the thinnest Be-backed Au film, while that of the glass was about 15% of the yield from the thinnest glass-backed film. After

subtraction of the substrate backscatter yields from those of the thin films, the resulting corrected yields were equal, within experimental error of about 2%, for corresponding films on glass and Be. This agreement was found over the primary energy range 50-110 keV and for various film thicknesses in the range 75-350 Å. It was, therefore, concluded that (1) corresponding films on glass and Be had the same thickness, and (2) the observed backscatter yields could be corrected by subtraction of the substrate yield.

The measured thicknesses of the five Au films are 75, 120, 170, 265, and 350 Å. These are estimated to be correct to within 5 Å.

CHAPTER IV

RESULTS

4:1 Backscatter of ^1H

The five Au films and the Be substrate were bombarded in succession by proton beams of the order of 10^{-10} A at various fixed primary energies in the range 50-110 keV. The total backscatter counts during 10 sec intervals were recorded for each film and the substrate at each primary energy. Just prior to and immediately after each counting interval the incident ion current was measured to an accuracy of better than 2%. If these two ion current measurements differed by more than 5%, the data were discarded. In order to minimize statistical errors a minimum total of 3000 backscatter events were recorded for each film at each energy. The gross backscatter yield, B^1 , was obtained by dividing the backscatter counts per second by the projectile particle current.

For a given film B^1 includes contributions from both the Au film and the substrate. At the highest primary energy the B^1 value of the substrate reached a maximum and equalled about 5% of the B^1 value of the thinnest Au film. The corrected backscatter yield, B_0 , was calculated (Sec 3:2) by subtracting the substrate yield from each recorded film yield. The energy dependence of the observed backscatter yield, B_0 , for the various Au films is presented in Fig. 4 by the solid curves through the points marked as circles. The dashed curves, which represent the same data corrected for energy loss in the films and for multiple small-angle scattering effects, will be discussed in Chapter VI.

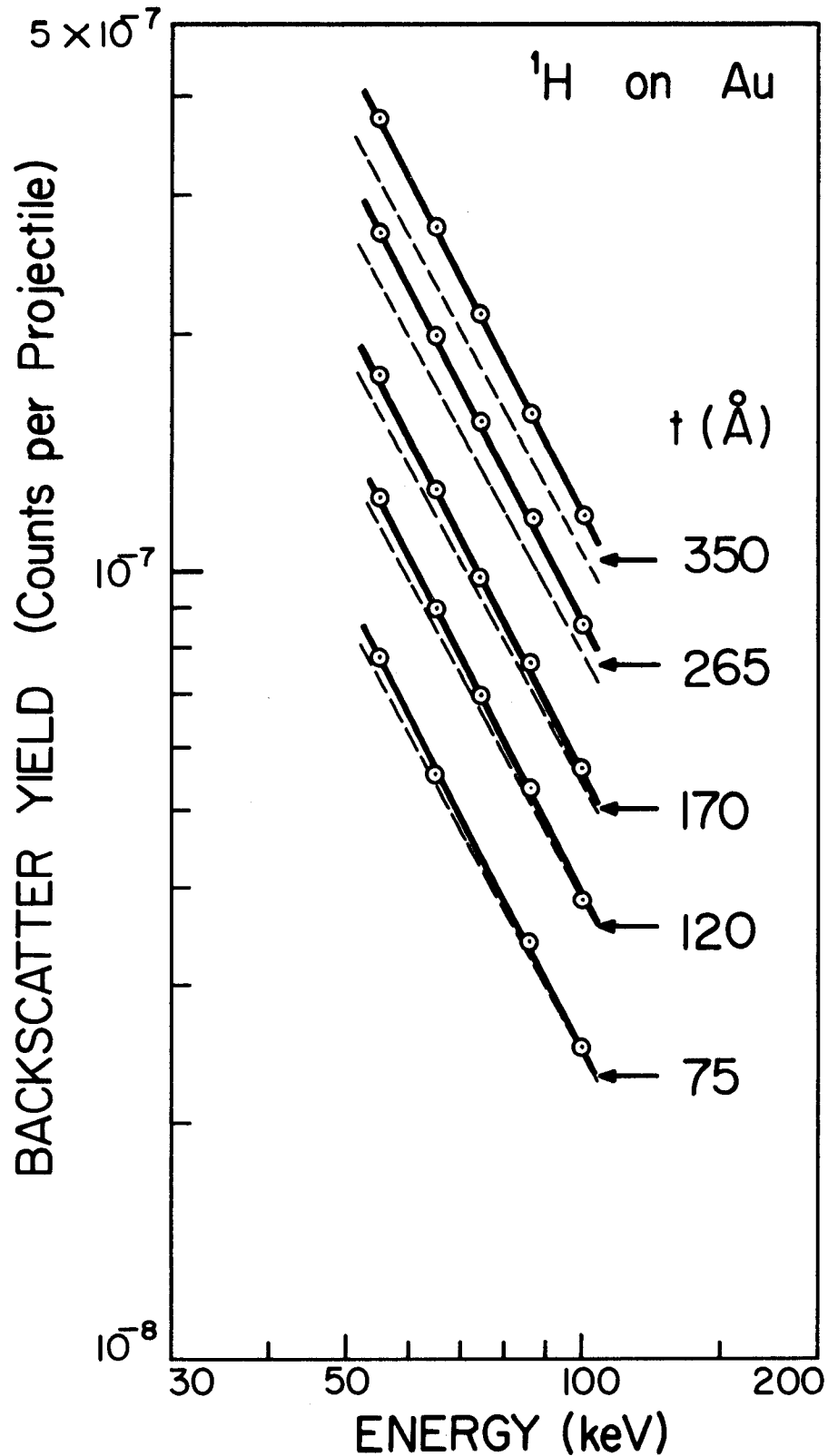


Figure 4. The solid curves through the experimental points (circles) show the dependence of the observed backscatter yield on primary energy for ^1H impinging on various gold films. The dashed curves, without experimental points, are plots of the corresponding backscatter yields corrected for multiple scattering effects versus the average energy.

4:2 Backscattering of ^4He , ^7Li , and ^{11}B

The five Au films and the Be substrate were also irradiated with monoenergetic beams of $^4\text{He}^+$, $^7\text{Li}^+$, and $^{11}\text{B}^+$ ions. With these projectiles the substrate yield was either zero, or negligible, being three orders of magnitude smaller than the thinnest film yield in the case of ^4He . The observed B_0 values for the various thin films are presented as circles in Figs. 5-7 as a function of primary energy. As the projectile mass increased, the primary energy for which 100% detection could be obtained increased rapidly, limiting the energy range of our investigations.

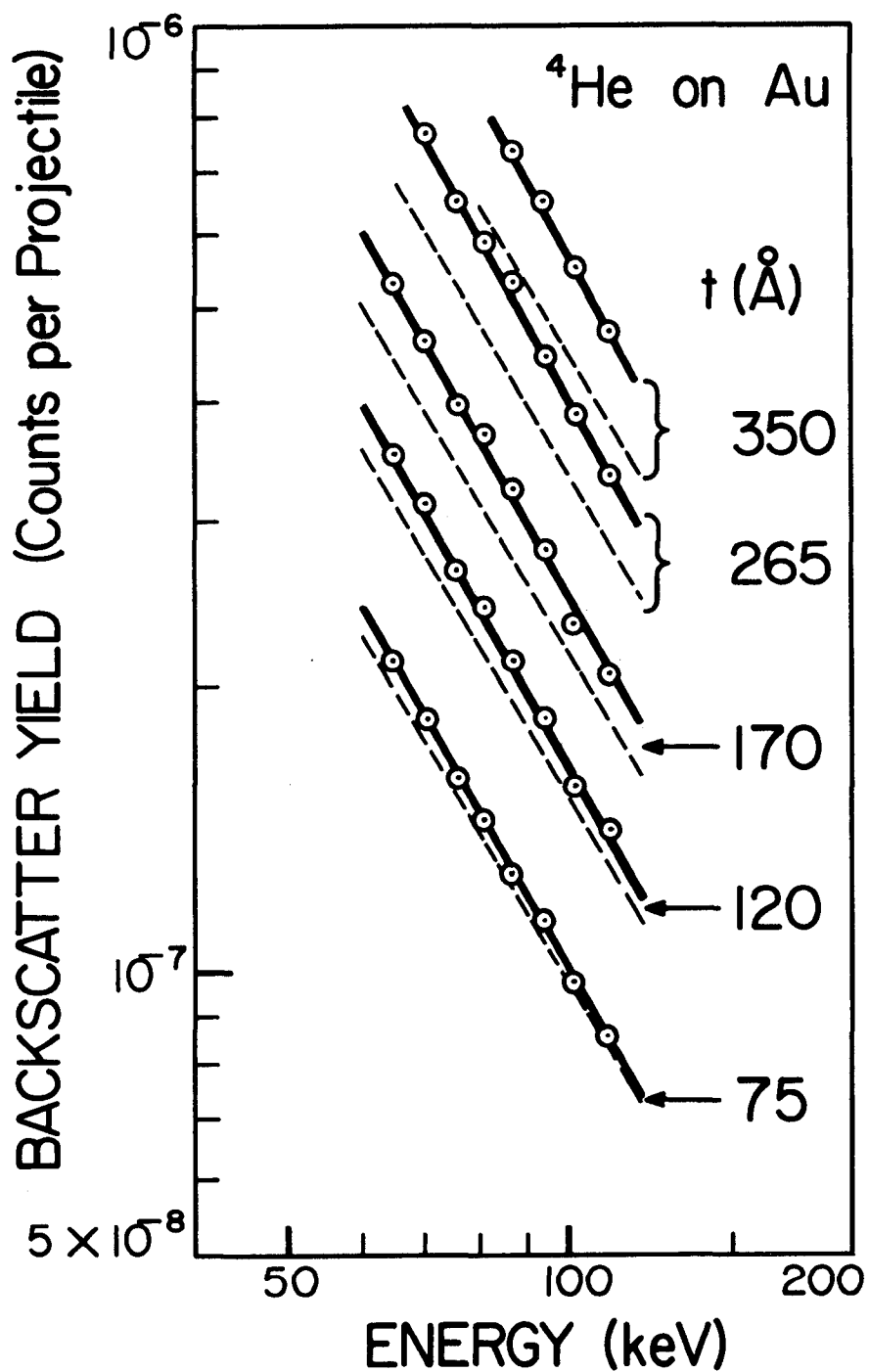


Figure 5. The solid curves through the experimental points (circles) show the dependence of the observed backscatter yield on primary energy for ${}^4\text{He}$ impinging on various gold films. The dashed curves, without experimental points, are plots of the corresponding backscatter yields corrected for multiple scattering effects versus the average energy.

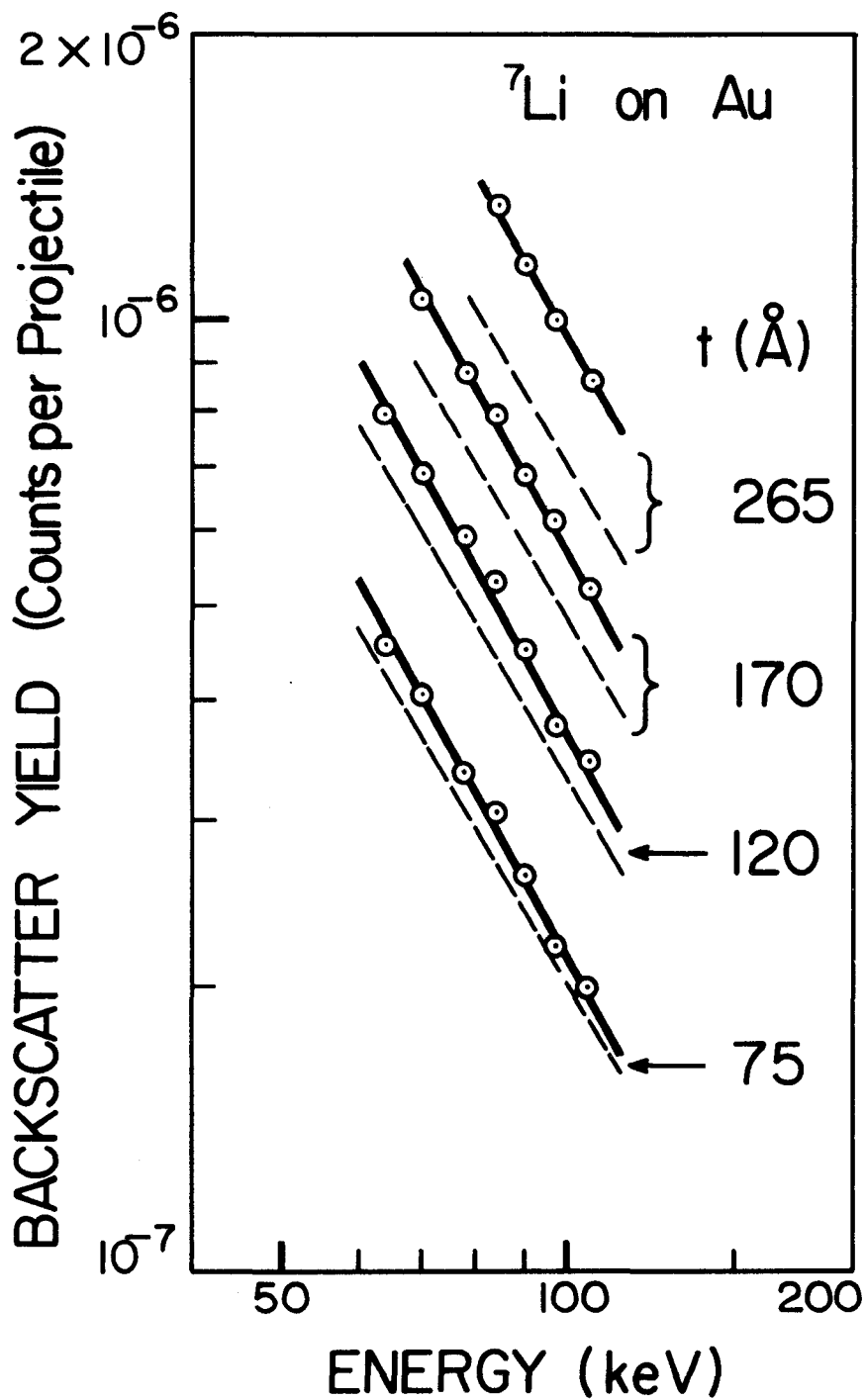


Figure 6. The solid curves through the experimental points (circles) show the dependence of the observed backscatter yield on primary energy for ${}^7\text{Li}$ impinging on various gold films. The dashed curves, without experimental points, are plots of the corresponding backscatter yields corrected for multiple scattering effects versus the average energy.

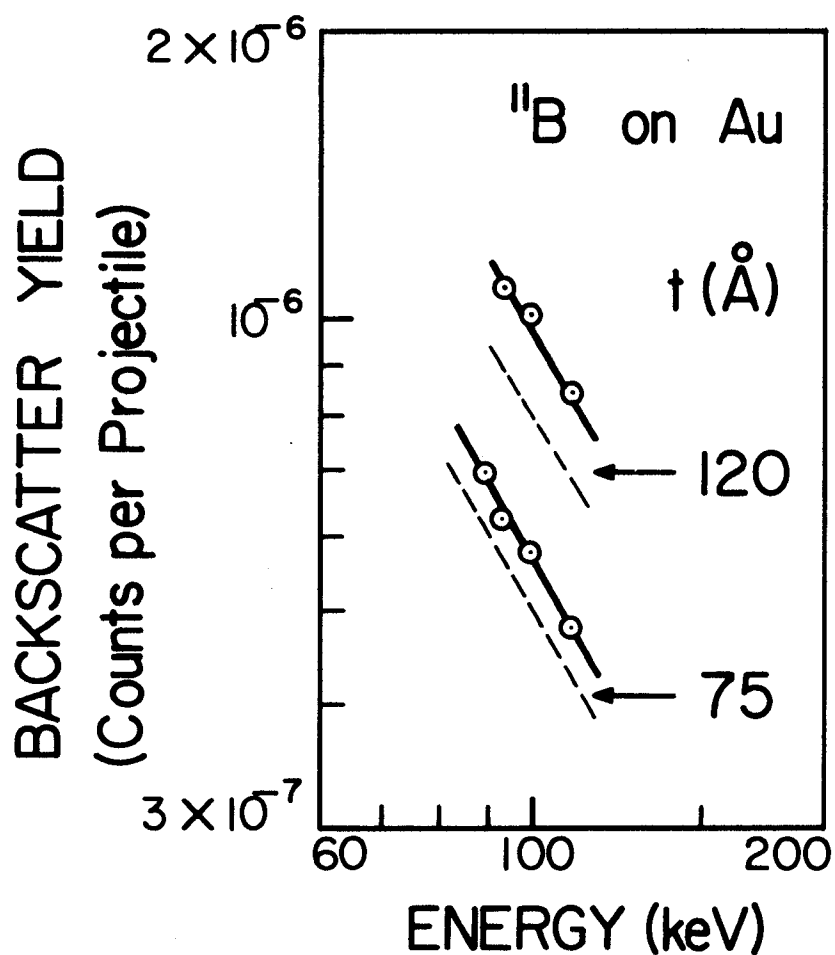


Figure 7. The solid curves through the experimental points (circles) show the dependence of the observed backscatter yield on primary energy for ^{11}B impinging on gold films of 75 Å and 120 Å thickness. The dashed curves, without experimental points, are plots of the corresponding backscatter yields corrected for multiple scattering effects versus the average energy.

CHAPTER V
ENERGY LOSS IN THE FILM

The observed B_0 value consists of projectiles backscattered anywhere inside the film material. Since the ion continually loses energy as it traverses the target medium, there is a range of energies over which the main scattering event can occur. In the absence of multiple scattering, the backscatter yield is directly proportional to film thickness, and on the average all violent collisions can be considered to occur at the centre of the thin film. To each B_0 value we assign an average energy of interaction $E = E_0 - \Delta E$, where E_0 is the primary energy and ΔE is the energy loss in one-half of the film thickness. The ΔE values have been computed using the energy-loss theory of Lindhard and Scharff (1961) (Lindhard et al. 1963). We shall now summarize some of the important aspects of this theory.

The total stopping power of a target material for a projectile is related to the total stopping cross section S by

$$\frac{dE}{dR} = NS \quad (13)$$

where N is the atomic density of the target medium. Although an energetic atomic projectile is deflected only by nuclear collisions (Bohr 1948), the energy of the projectile is dissipated to both electrons and recoiling atoms in the stopping medium. Thus the total stopping cross section consists of the stopping cross section S_n for loss in energy in nuclear collisions and the stopping cross section S_e for loss in energy to electrons:

$$S = S_e + S_n \quad (14)$$

From Eqs. 13 and 14 we see that

$$\frac{dE}{dR} = \left(\frac{dE}{dR}\right)_n + \left(\frac{dE}{dR}\right)_e \quad (15)$$

where $\left(\frac{dE}{dR}\right)_n = NS_n$ and $\left(\frac{dE}{dR}\right)_e = NS_e$. (16)

To obtain a universal description for energy loss, which is valid for all atomic projectile-target combinations, Lindhard et al. introduced the dimensionless variables

$$\epsilon = E \frac{am_2}{Z_1 Z_2 e^2 (m_1 + m_2)} \quad (17)$$

and $\varphi = R \frac{Nm_2 4\pi a^2 m_1}{(m_1 + m_2)^2}$ (18)

for energy and range respectively. In terms of these variables Eqs. 16 can be written as

$$\left(\frac{dE}{dR}\right)_n = \frac{4\pi a Z_1 Z_2 e^2 N m_1}{(m_1 + m_2)} \left(\frac{d\epsilon}{d\varphi}\right)_n \quad (19)$$

and $\left(\frac{dE}{dR}\right)_e = \frac{4\pi a Z_1 Z_2 e^2 N m_1}{(m_1 + m_2)} \left(\frac{d\epsilon}{d\varphi}\right)_e$. (20)

Lindhard et al. present a universal curve (Fig. 8) for $\left(\frac{d\epsilon}{d\varphi}\right)_n$ versus $\epsilon^{\frac{1}{2}}$ which is based on the Thomas-Fermi statistical model of the colliding atoms. In terms of the new variables the electronic stopping power is given by

$$\left(\frac{d\epsilon}{d\varphi}\right)_e = K \epsilon^{\frac{1}{2}} \quad (21)$$

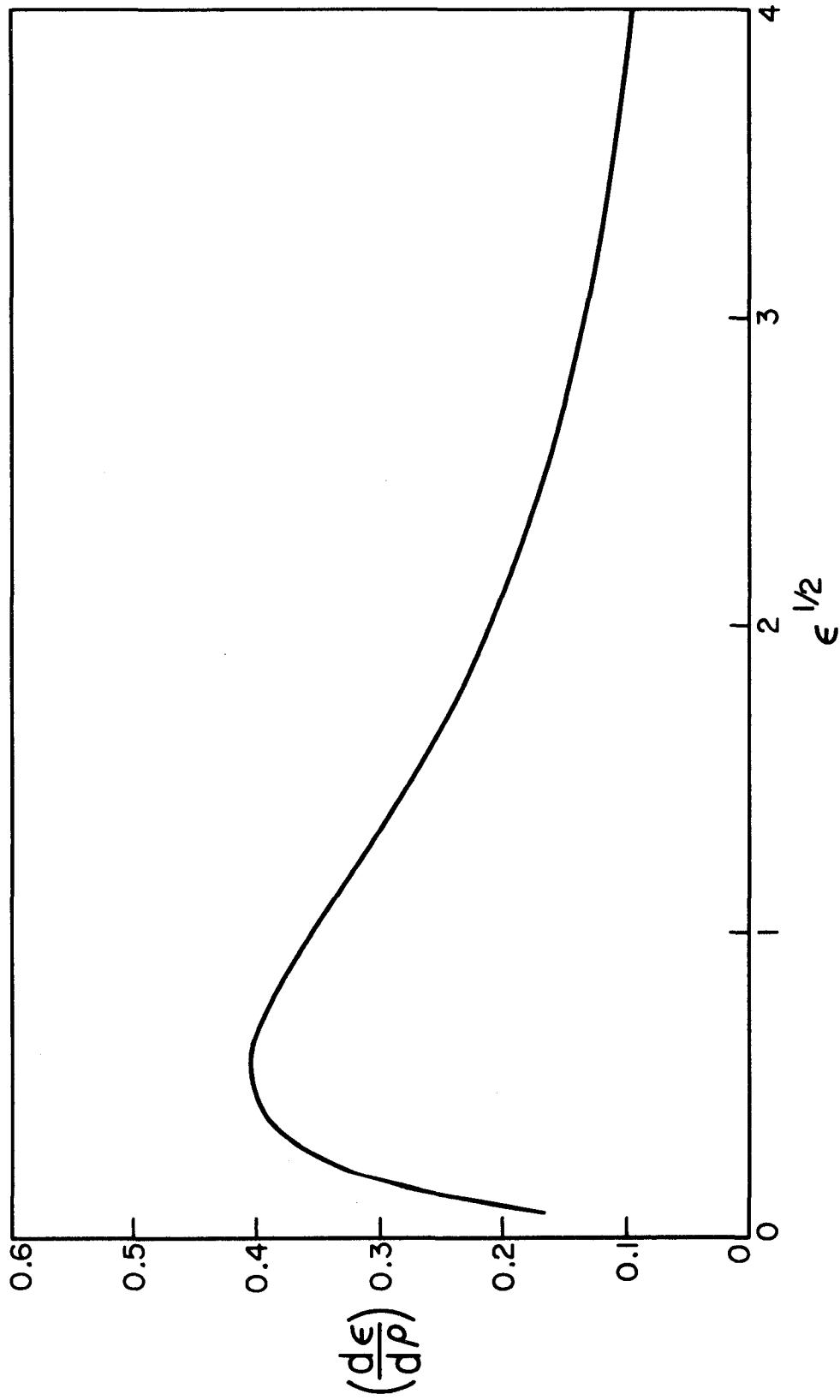


Figure 8. The nuclear stopping power $(\frac{d\epsilon}{d\rho})_n$ as a function of $\epsilon^{1/2}$ (from Lindhard et al. 1963).

where

$$K = Z_1^{1/6} \frac{0.0793 Z_1^{1/2} Z_2^{1/2} (A_1 + A_2)^{3/2}}{(Z_1^{2/3} + Z_2^{2/3})^{3/4} A_1^{3/2} A_2^{1/2}} \quad (22)$$

in which A_1 and A_2 are the atomic numbers of the projectile and target atoms respectively. The values of K for ^1H , ^4He , ^7Li and ^{11}B on Au are 15.13, 3.00, 1.71, and 1.216 respectively. Thus using Fig. 8 for $\left(\frac{d\epsilon}{d\rho}\right)$ and Eqs. 21 and 22 for $\left(\frac{d\epsilon}{d\rho/e}\right)$, one can compute the $\frac{dE}{dR}$ values from

Eqs. 15, 19 and 20.

The energy loss ΔE in a thin stopping region of thickness ΔR (much smaller than the range of the projectile) is then found from the relationship

$$\Delta E \approx \left(\frac{dE}{dR}\right) \Delta R \quad (23)$$

where

$$\Delta E = \Delta E_n + \Delta E_e, \quad (24)$$

$$\Delta E_n \approx \left(\frac{dE}{dR}\right)_n \Delta R, \quad (25)$$

and

$$\Delta E_e \approx \left(\frac{dE}{dR}\right)_e \Delta R. \quad (26)$$

The simple analytic form (Eq. 21) applies only for projectile velocities $v \lesssim v_1 = v_0 Z_1^{2/3}$ where v_0 is the velocity of an electron in the first Bohr orbit of ^1H . Only at these low velocities ($v < v_1$) is the electronic stopping nearly proportional to v . The upper limit for the validity of the Lindhard and Scharff theory therefore increases with projectile mass, being ~ 25 keV for protons and ~ 250 keV for ^4He . For protons travelling in Au, however, the theory is in agreement with experiment (see Whaling 1958, and references contained therein) up to

energies of 120 keV, allowing us to compute ΔE for protons as well as for heavier projectiles over the entire energy range investigated.

For velocities $v > v_1 = v_0 Z_1^{2/3}$ electronic stopping completely dominates, but it is no longer proportional to v . For $v < v_1$ electronic stopping still dominates for $Z_1 < Z_2$. For heavier projectiles and or decreasing energy, nuclear stopping gradually overtakes electronic stopping to become the major mechanism of energy loss. However even for our heaviest projectile (^{11}B), ΔE_e remains a factor of 4 larger than ΔE_n . For this reason the model described by McCracken and Freeman (1969), where the incident ion travels in straight lines except for violent collisions, should be correct to a first approximation for light ions.

The average ΔE values in the thinnest film are 0.7 keV for protons, ~ 1 keV for ^4He and ^7Li and ~ 1.8 keV for ^{11}B . Even large uncertainties in these small energy corrections still allows us to obtain the average energy of interaction, $E = E_0 - \Delta E$, to a sufficiently high degree of precision.

CHAPTER VI

MULTIPLE SCATTERING EFFECTS

If the incident ions travelled straight-line paths in the target material until they suffered a single violent interaction and were scattered, and then proceeded rectilinearly out of the stopping medium, only particles scattered into $\Delta\Omega = 5.25 \times 10^{-4}$ sr about $\theta_L = 136.4^\circ$ would reach the detector. As a consequence of multiple small-angle scatterings before the violent collision, the beam gradually spreads out about the direction of initial incidence. In any infinitesimal time interval dT , there is a probability $\sigma(\theta, E)dT$ for each particle to be scattered back, where θ is the scattering angle with respect to the direction of motion immediately preceding scattering and E is the projectile energy at that instant. The projectile density in the diverging beam is azimuthally isotropic. Because the Rutherford cross section is highly preferred in the forward direction, particles travelling at angles $\theta < \theta_L = 136.4^\circ$ with respect to the detector are more likely to enter the detector than those with $\theta > \theta_L$. Consequently more particles are multiply-scattered into the solid angle of the detector than out of it, resulting in an enhancement of the backscatter yield. Backscattered particles also suffer small deflections, further enhancing the backscatter yield. To compare the observed backscatter yield with the theoretically predicted one for a single scattering event, a correction must be applied to B_0 .

6:1 Angular Divergence

To find the correction factor by which the observed backscatter yield must be divided in order to correct for multiple small-angle deflections, an estimate of the angular divergence of the beam in travelling through a thin stopping region is required. Suppose the projectile encounters several scattering centers on its passage through the stopping medium. Since the individual deflections are completely random, the average deflection is zero. The root-mean-square (rms) deflection will not vanish, however, since there exists a random walk in angle away from the direction of initial incidence. The total rms deflection associated with the projectile penetrating a depth ΔR into the medium can be estimated as follows. Consider an elastic collision between two atoms in which the particles are deflected through the common angle of scattering θ in the CM system. From Appendix III the projectile (m_1) transfers an amount of energy to the recoiling target (m_2) equal to

$$T = \frac{4m_1m_2}{(m_1 + m_2)^2} E \sin^2(\theta/2), \quad (27)$$

where E is the impact energy. For light projectiles ($m_1 \ll m_2$), the lab and CM systems are almost identical, and $\theta \simeq \theta_0$. Since the vast majority of collisions are small-angle ones Eq. 27 reduces to

$$T \simeq 4(m_1/m_2)E(\theta/2)^2. \quad (28)$$

When a swift ion traverses a thin stopping region, it undergoes several small deflections from its original direction of motion, losing an amount of energy

$$\Delta E_n = \sum_i T_i \quad (29)$$

in atomic recoils, where the summation includes all scattering events. Substituting for T_i from Eq. 28, the nuclear energy loss becomes

$$\Delta E_n \simeq (m_1/m_2) \sum_i E_i \theta_i^2 \simeq (m_1/m_2) E \sum_i \theta_i^2 \quad (30)$$

where E_i is the projectile energy prior to the i^{th} collision. In a thin film the projectile energy remains nearly constant and has, therefore, been taken outside the summation sign. If all scattering angles are small, the resulting angular distribution is approximately gaussian (Bohr, 1948) with a root-mean-square width

$$\phi_{\text{rms}} \simeq \sqrt{\sum_i \theta_i^2} \simeq \sqrt{\frac{1}{E} \frac{m_2}{m_1} \Delta E_n} \quad (31)$$

The calculation of ΔE_n has been described in the previous Chapter. Because all scattering events are not small angle ones, the actual angular distribution will differ from a gaussian. Eq. 31 is, therefore, considered to be only a rough estimate of the angular divergence.

6:2 Correction Factor

The correction factor ($CF = B_0/B$) is the factor by which the observed backscatter yield, enhanced by the effects of multiple small-angle scattering, must be divided to obtain the yield that would be observed at a laboratory scattering angle $\theta_L = 136.4^\circ$ in the absence of multiple deflections. The correction factor was estimated, by means of a computer program, using the following assumptions:

(1) The Rutherford cross section gives the form of the backscattered angular distribution. Since for large scattering angles the shape of the angular distribution is but little affected by electronic screening, this assumption introduces only small errors.

(2) All backscatter events occur at a film depth $\Delta R = t/2$ where t is the film thickness.

(3) Just prior to backscattering the incident ions are distributed over an angular distribution of gaussian form, centered about the incident direction, whose rms width is given by Eq. 31 with $\Delta R = t/2$.

(4) As the backscattered ions travel out of the film they again spread out in a gaussian angular distribution about their original scatter directions, with an rms width at the film surface again given by Eq. 31 but with $\Delta R = (t/2) \sqrt{2}$, the average distance the ions travel through the film after being scattered from the film center towards the detector.

The results of the computation are presented in Fig. 9 as a plot of the correction factor versus ϕ , the predicted rms width of the angular distribution for $\Delta R = t/2$. The correction factor was found to be slightly small. A better one was obtained by replacing ϕ , as calculated from Eq. 31, with 1.10ϕ and reading the correction factor from the same curve (Fig. 9). The new values were found to be adequate (See Section 6:3) for all film thicknesses and all projectiles at all energies investigated.

The dependence of B (the B_0 value corrected for multiple scattering effects) on the average energy of interaction (the primary energy corrected for energy loss in the film) is represented by the

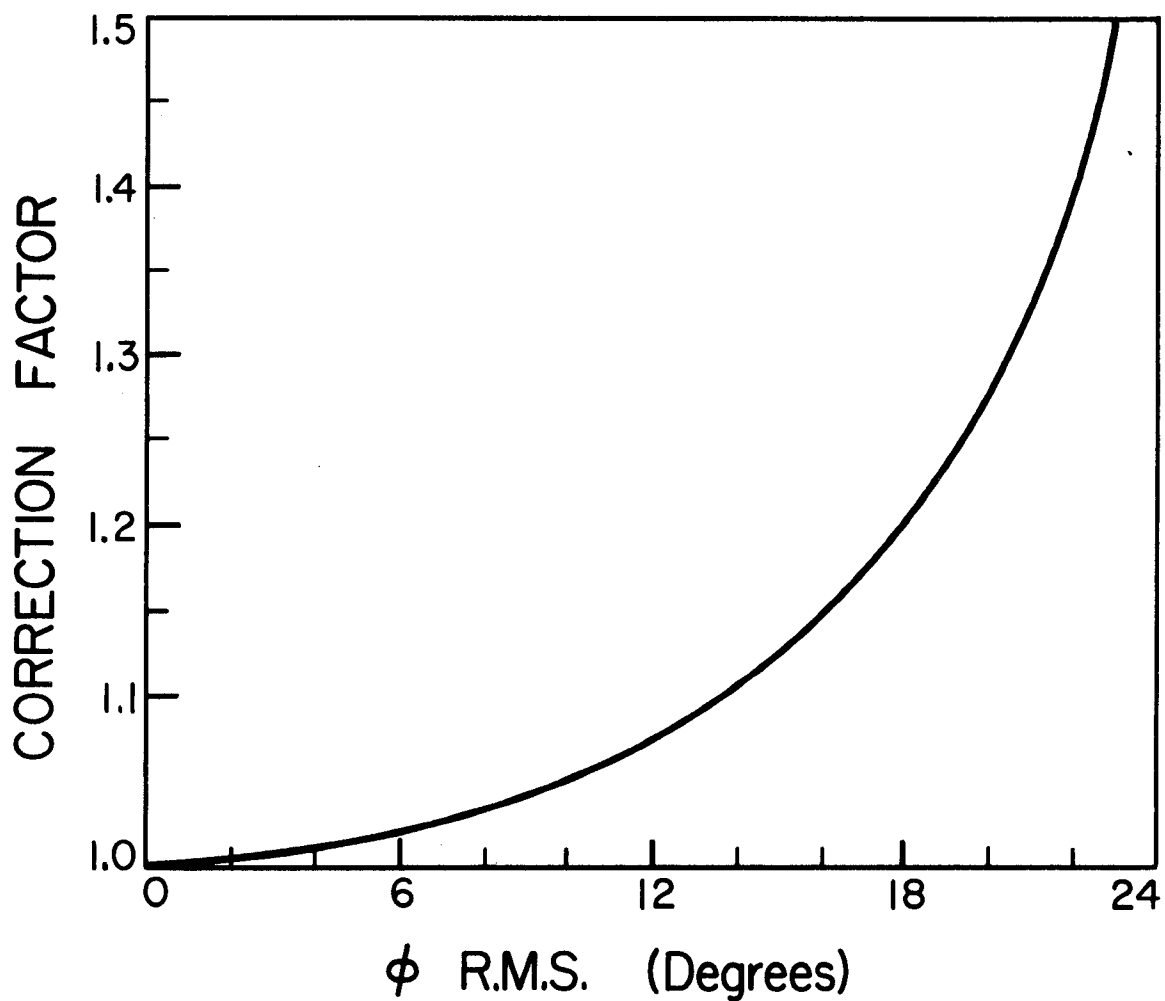


Figure 9. Correction factor for multiple scattering as a function of ϕ_{rms} evaluated at half the film thickness.

dashed curves in Figs. 4-7. Both axes in each of these diagrams have a dual meaning. The abscissa represents the primary energy E_0 for the solid curves, and the average energy $E = E_0 - \Delta E$ for the dashed curves. The ordinate represents the observed backscatter yield B_0 for the solid curves, and the corrected yield $B = B_0/CF$ for the dashed curves.

6:3 Dependence of Backscatter Yield on Film Thickness

The dependence of the observed backscatter yield B_0 on the measured film thicknesses at an average interaction energy of 100 keV is shown by the dashed curves through the experimental points marked as squares in Fig. 10. Since smooth curves can be fitted quite nicely through these points, the film thickness measurements appear to be accurate well within the uncertainty of $\pm 5 \text{ \AA}$.

In the absence of multiple scattering the backscatter yield should be proportional to film thickness for t values much smaller than the range of the projectile in the film. The circles in Fig. 10 represent the same data as the squares, but the ordinate now represents the yield corrected for multiple deflections ($B = B_0/CF$). Straight lines (the solid curves) passing through the origin provide good fits to the B values, indicating that the correction factor for multiple deflections may be fairly accurate. It will be noticed that multiple scattering effects increase rapidly with increasing projectile mass. The reason for this is that the ratio $\Delta E_n/m_1$ (See Eq. 31) increases with projectile mass.

The error in the correction factors is difficult to estimate, but the deviations from unity of these factors appear to be accurate to, at least, within 20%. For the thinnest film the average correction

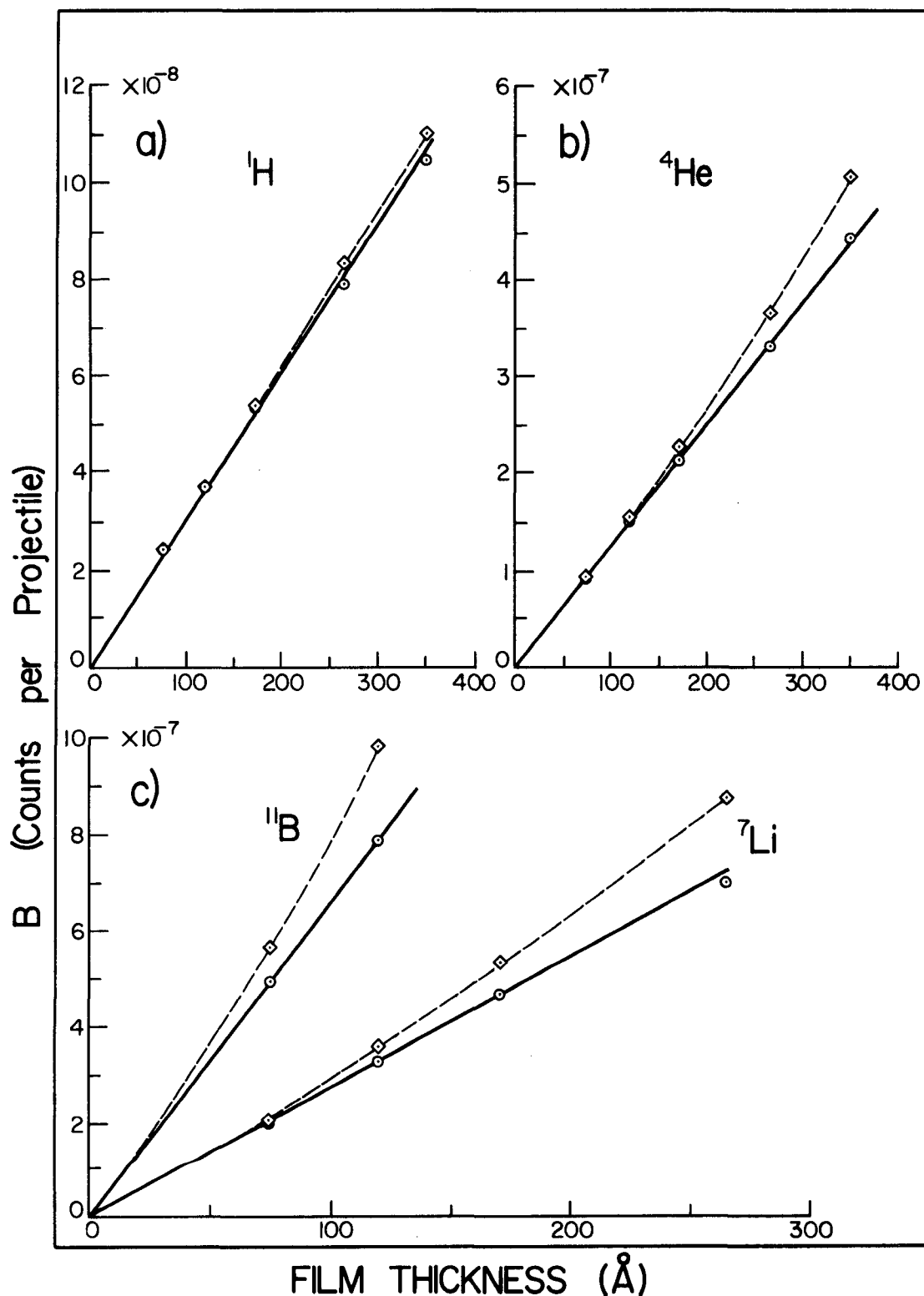


Figure 10. Each of these diagrams is a composite showing (1) the thickness dependence of the experimental backscatter yield (squares) for the indicated projectile on Au, at an energy $E = 100$ keV, and (2) the thickness dependence of the corresponding backscatter yield (circles) corrected for multiple scattering effects.

factors in the energy range investigated are 1.02, 1.03, 1.05 and 1.12 for ^1H , ^4He , ^7Li and ^{11}B respectively. A 20% error in the deviations from unity of these numbers results in a change in B of less than 1% for the three lightest projectiles and less than 3% for the fourth. We conclude, therefore, that the uncertainties in B introduced by multiple scattering are practically negligible for the thinnest film.

CHAPTER VII

DISCUSSION

Because the data for the thinnest film are the most certain, only the 75 Å film results will be compared with theory. The laboratory backscatter cross section is given by (See Appendix IV)

$$\frac{d\sigma}{d\Omega} \approx \frac{B}{N(\Delta\Omega)t} \quad (32)$$

where $\Delta\Omega$ is the solid angle subtended by the detector and N is the atomic density of the stopping medium. The cross sections for the various projectiles were calculated at each energy investigated by substitution of numerical values into Eq. 32. The cross sections for ^1H near 100 keV were found to be 1.03 times the values predicted by the shell-shielded Coulomb potential with a replaced by $2a$ (Eq. 12). Since the conversion from B value to cross section involves the measured value of the film thickness and its uncertainty, and the statistical error in B (less than 2%), no physical significance can be attributed to such a factor. The observed cross sections for all projectiles have been divided by 1.03. This normalizes the theoretical and experimental values for ^1H at 100 keV. The normalized cross sections are presented as circles in Fig. 2. The solid curves provide fairly accurate fits to the data, both in magnitude and energy dependence. The shell-shielded Coulomb potential, therefore, quite accurately describes the interaction involved in backscattering of light atomic projectiles in the energy range investigated.

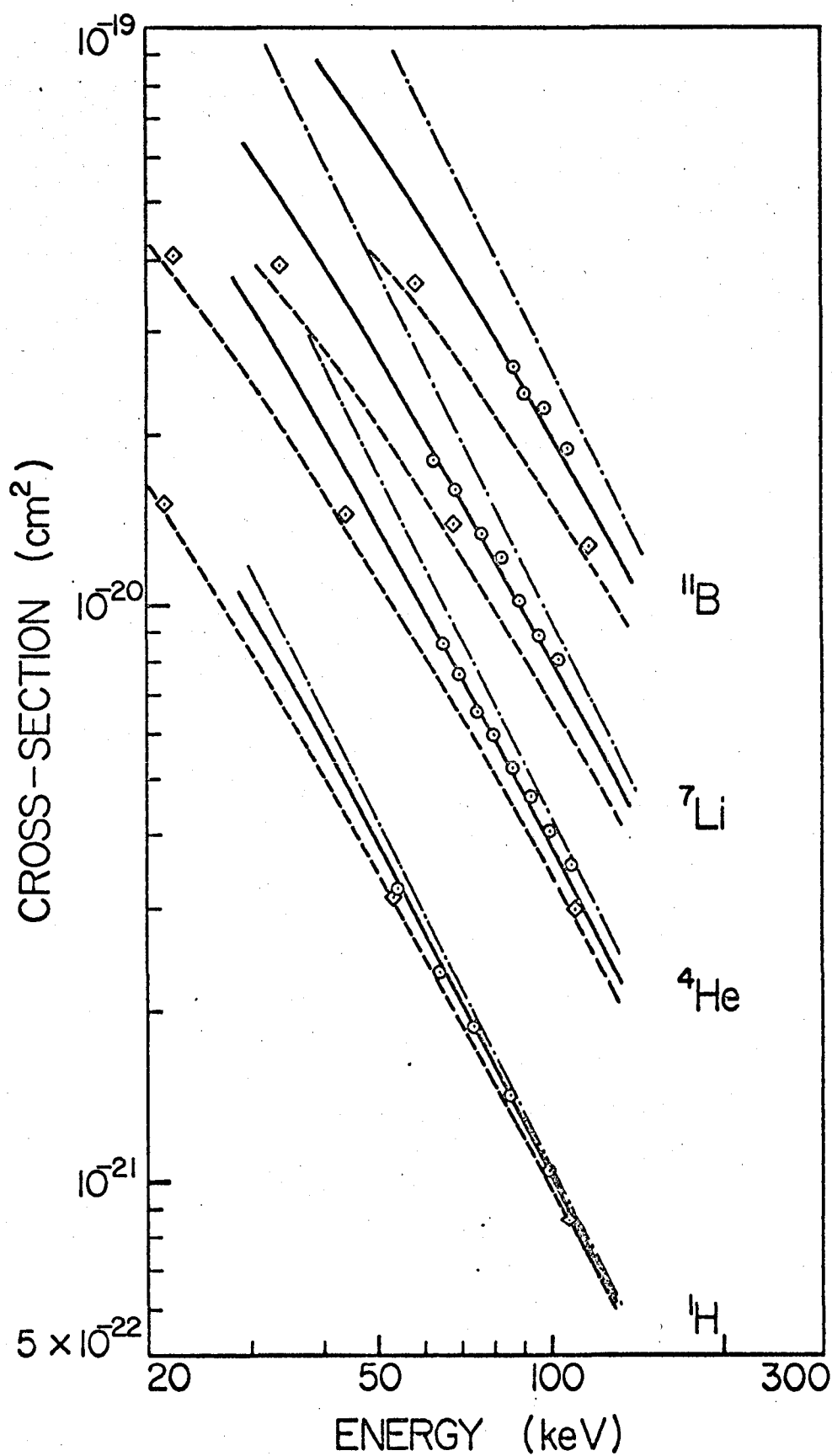


Figure 2. Energy dependence of lab cross sections at $\theta_L = 136.4^\circ$ for various projectiles on gold. - · - · Rutherford; — shell-shielded Coulomb $a \rightarrow 2a$; - - - shell-shielded Coulomb; \diamond screened Coulomb; \circ experimental.

APPENDIX 1

THE SHELL SHIELDED COULOMB POTENTIAL

Consider a potential

$$\phi(R) = (Q/R) (1-R/a) H(1-R/a) \quad (7)$$

where $H(x)$ is the Heaviside step function.

Define $U(R) = R \phi(R) = Q (1-R/a) H(1-R/a)$.

The charge distribution $\rho(R)$ giving rise to this potential $\phi(R)$ is given by Poisson's equation

$$\nabla^2 \phi = -4\pi \rho(R).$$

For $R > a$, $\nabla^2 \phi$ vanishes since ϕ does.

For $R < a$, $\nabla^2 \phi = -4\pi Q \delta(\vec{R})$

For $R = a$, $\nabla^2 \phi = \frac{1}{R} \frac{d^2}{dR^2} [R \phi(R)] \Big|_{R=a} = \frac{1}{R} \frac{d^2}{dR^2} U(R) \Big|_{R=a}$

Here $\delta(R)$ is the Dirac delta function.

Therefore the total $\nabla^2 \phi(R) = \frac{1}{R} U''(a) - 4\pi Q \delta(\vec{R})$

Note: $U''(R) = 0$ everywhere except at $R = a$.

To find $U''(a)$, let $x = (1-R/a)$.

Then $\frac{d^2}{dR^2} = \frac{1}{a^2} \frac{d^2}{dx^2}$

and $\frac{1}{R} \frac{d^2}{dR^2} U = \frac{Q}{Ra^2} \frac{d^2}{dx^2} [xH(x)]$

$$= \frac{Q}{Ra^2} [2 \delta(x) + x \delta'(x)] \quad \text{since } H'(x) = \delta(x).$$

$$= \frac{Q}{Ra^2} \delta(x) \quad \text{since } f(x) \delta'(x) = -\delta(x) f'(x)$$

$$= \frac{Q}{Ra^2} \delta(1-R/a)$$

$$= \frac{Q}{Ra} \delta(R-a) \quad \text{since } \delta(x) = a \delta(ax)$$

$$\text{and } \delta(x) = \delta(-x)$$

$$= \frac{Q}{a^2} \delta(R-a) \quad \text{since } \delta(x) = 0 \text{ unless } R=a.$$

Therefore $\nabla^2 \phi(\vec{R}) = \frac{Q}{a^2} \delta(R-a) - 4\pi Q \delta(\vec{R})$

$$= -4\pi e,$$

and the charge distribution is

$$e = Q \delta(\vec{R}) - Q(4\pi a^2)^{-1} \delta(R-a),$$

corresponding to a point charge Q at the centre of a spherical shell (radius a) of surface charge density $-Q(4\pi a^2)^{-1}$.

APPENDIX 11

THE CLASSICAL CROSS SECTION FOR THE SHELL-SHIELDED COULOMB POTENTIAL

The validity of the classical calculation has been discussed by Bohr (1948) and by Mott and Massey (1965). For a classical treatment to be valid, two conditions must be satisfied:

- (1) $\lambda \ll a, \lambda \ll b$ where λ is the de Broglie wavelength of the projectile,
 b is the collision diameter,
and a is the screening length.
- (2) $\theta > \lambda/2\pi a$ (See Bohr).

For the cases treated in this thesis (H, He, Li, and B at 50-110 keV on Au), the classical calculation is valid at all scattering angles $\theta > 0.1^\circ$.

The classical differential scattering cross section,

$$\frac{d\sigma}{d\Omega} = \frac{2\pi p dp}{2\pi \sin\theta d\theta} = \frac{1}{2} \frac{d(p^2)}{d(\cos\theta)} = \frac{1}{4} \left[\frac{d(\sin^2\theta/2)}{d(p^2)} \right]^{-1} \quad (33)$$

for a central potential, can be calculated from the relationship between the Center-of-Mass (CM) scattering angle θ and the impact parameter p . From the conservation of energy Goldstein (1959) finds

$$\theta = \pi - 2 \int_0^{y_0} dy / \sqrt{1 - V(p/y)/E - y^2} \quad (34)$$

where $y = p/R$ and $y_0 = p/R_0$. Here R_0 is the turning point of the orbit, determined by

$$E = L^2/2uR^2 + V(R_0) = Ep^2/R + V(R_0) \quad (35)$$

where E is the CM energy, u is the reduced mass and L is the angular momentum.

In terms of the new variable y and the parameter $Q = Z_1 Z_2 e^2$ the potential (Eq. 7)

$$\begin{aligned} V(R) &= Q/R (1-R/a), & 0 \leq R \leq a \\ &= 0, & R > a \end{aligned} \quad (7)$$

becomes

$$\begin{aligned} V(p/y) &= Qy/p (1-p/ya), & y \geq p/a \\ &= 0, & y < p/a \end{aligned}$$

Substitution of this potential into Eq. 34 yields

$$\theta = \pi - 2 \int_0^{p/a} dy / \sqrt{1-y^2} - 2 \int_{p/a}^{y_0} dy / \sqrt{1 - Qy(1-p/ya)/(pE) - y^2}.$$

With $w = Ea/Q$, and $c = p/a$, we obtain

$$\begin{aligned} \theta &= \pi - 2 \int_0^c dy / \sqrt{1-y^2} - 2 \int_c^{y_0} dy / \sqrt{1 + (1-y/c)1/w - y^2} \\ &= \pi - 2 \operatorname{Arcsin} y \Big|_0^c - 2 \operatorname{Arcsin} \left[(2y + 1/wc) / \sqrt{(wc)^{-2} + 4 + 4/w} \right] \Big|_{y=c}^{y=y_0} \end{aligned}$$

Using Eq. 35, the upper limit y_0 becomes

$$2y_0 = -1/wc + \sqrt{(wc)^{-2} + 4 + 4/w}$$

On substitution of this value into the previous equation, we find

$$\begin{aligned} \theta &= 2 \operatorname{Arcsin} \left[(1 + 2wc^2) / \sqrt{1 + (2wc)^2(1 + 1/w)} \right] - 2 \operatorname{Arcsin} c \\ &= 2 (A-B) \end{aligned}$$

where $\sin A = (1 + 2wc^2) / \sqrt{1 + (2wc)^2 (1 + 1/w)}$

$$\cos A = 2wc \sqrt{1-c^2} / \sqrt{1 + (2wc)^2 (1 + 1/w)}$$

$$\sin B = c$$

$$\cos B = \sqrt{1-c^2}$$

From the previous equations it follows that

$$\sin \theta/2 = \sin(A-B) = \sin A \cos B - \cos A \sin B$$

$$= \sqrt{\frac{1-c}{1 + (2wc)^2 (1 + 1/w)}}, \quad (36)$$

and

$$\begin{aligned} \frac{d(\sin^2 \theta/2)}{d(p^2)} &= \frac{1}{a^2} \frac{d(\sin^2 \theta/2)}{d(c^2)} \\ &= \frac{1}{a^2} \left[\frac{1 + 2w}{1 + (2wc)^2 (1 + 1/w)} \right]^2 \\ &= \frac{1}{a^2} \left[\frac{1 + 2w}{1 - c^2} \right] \sin^4(\theta/2). \end{aligned}$$

The last step is easily verified by substituting for $\sin^4(\theta/2)$ (Eq. 36).

Thus the differential scattering cross section (Eq. 33) becomes

$$\frac{d\sigma}{d\Omega} = \frac{a^2}{4} \left[\frac{1-c^2}{1-2w} \right]^2 \csc^4(\theta/2). \quad (37)$$

In terms of the quantities $Q (= Z_1 Z_2 e^2)$ and $w (= Ea/Q)$, the collision diameter is given by $b = a/w$, and the Rutherford cross section becomes

$$\left(\frac{d\sigma}{d\Omega}\right)_R = (b/4)^2 \csc^4(\theta/2) = \left(\frac{a}{4w}\right)^2 \csc^4(\theta/2)$$

which allows us to rewrite Eq. 37 in the form

$$\begin{aligned} \frac{d\sigma}{d\Omega} &= 4 \left[\frac{1-c^2}{1+2w} \right] w^2 \left(\frac{d\sigma}{d\Omega}\right)_R \\ &= k \left(\frac{d\sigma}{d\Omega}\right)_R \end{aligned}$$

where $k^{1/2} = 2w(1-c^2)/(1+2w)$ (38)

With the aid of Eq. 36, the k value becomes

$$k = \left[\frac{1 + b/(2a)}{1 + b/a + b^2/(4a^2 \sin^2 \theta/2)} \right]^2 \quad (9)$$

and the differential cross section is

$$\frac{d\sigma}{d\Omega} = k \left(\frac{d\sigma}{d\Omega}\right)_R = \left[\frac{ab(a+b/2)}{4a \sin^2(\theta/2)(a+b) + b^2} \right]^2 \cdot \quad (8)$$

APPENDIX III

TRANSFORMATION FORMULAE BETWEEN LAB AND CM FRAMES

Because the experimentalist takes measurements in the laboratory (lab) system, and the theoretician finds it simpler to make his calculations in the Center-of-Mass (CM) system, conversion formulae from one frame of reference to the other are necessary.

Consider a nonrelativistic binary elastic collision which asymptotically appears in the lab system as in Fig. 11.

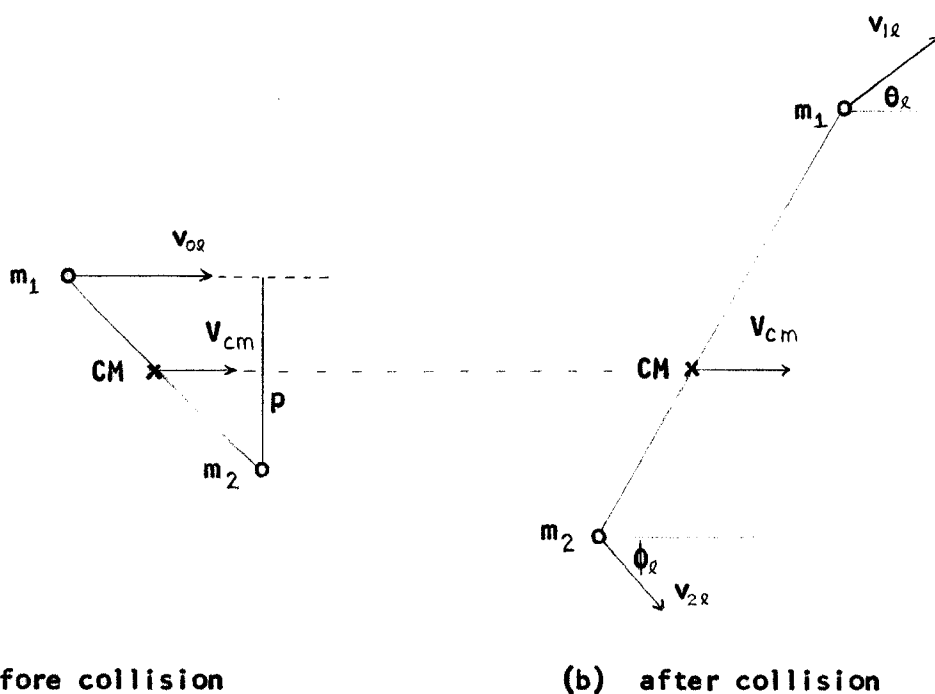


Fig. 11. Asymptotic views of an elastic collision in the lab system. Initially a particle of mass m_1 is moving with velocity v_{0l} and impact parameter p towards a particle of mass m_2 at rest in the lab frame. After scattering through angles θ_l and ϕ_l , m_1 and m_2 have velocities v_{1l} and v_{2l} respectively. In the lab frame the center of mass of the

two particles moves with constant velocity \bar{V}_{CM} . The magnitude and direction of \bar{V}_{CM} are determined by the conservation theorem for total linear momentum

$$(m_1 + m_2)\bar{V}_{CM} = m_1\bar{v}_{O\ell}$$

The CM system moves with respect to the lab system so that the origin of the CM system is always coincident with the center of mass of the colliding particles. In the CM frame the total energy is

$$E = E_\ell - \frac{1}{2}(m_1 + m_2)V_{CM}^2 = \frac{m_2}{m_1 + m_2} E_\ell$$

Because the total linear momentum is zero at all times in this frame, the particles are travelling in opposite directions to one another before and after the collision. Hence they share a common angle of scattering, θ (Fig. 12).

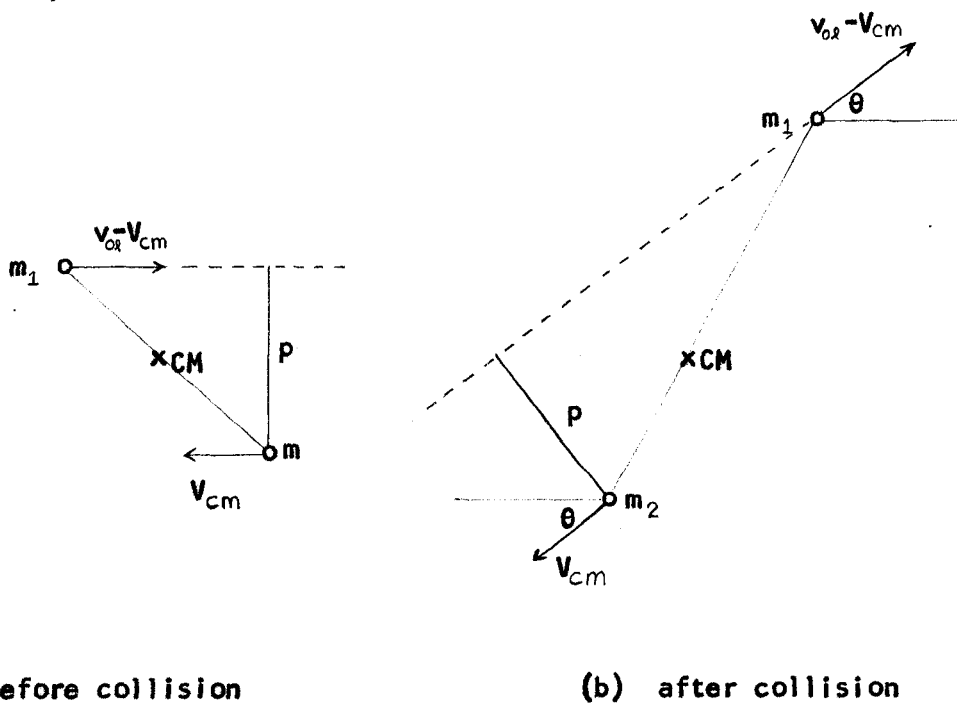


Fig. 12. Asymptotic views of an elastic collision in the CM system.

From a vector addition diagram relating the final velocities in the CM and lab frames, the relationship between the CM and lab scattering angles can be obtained.

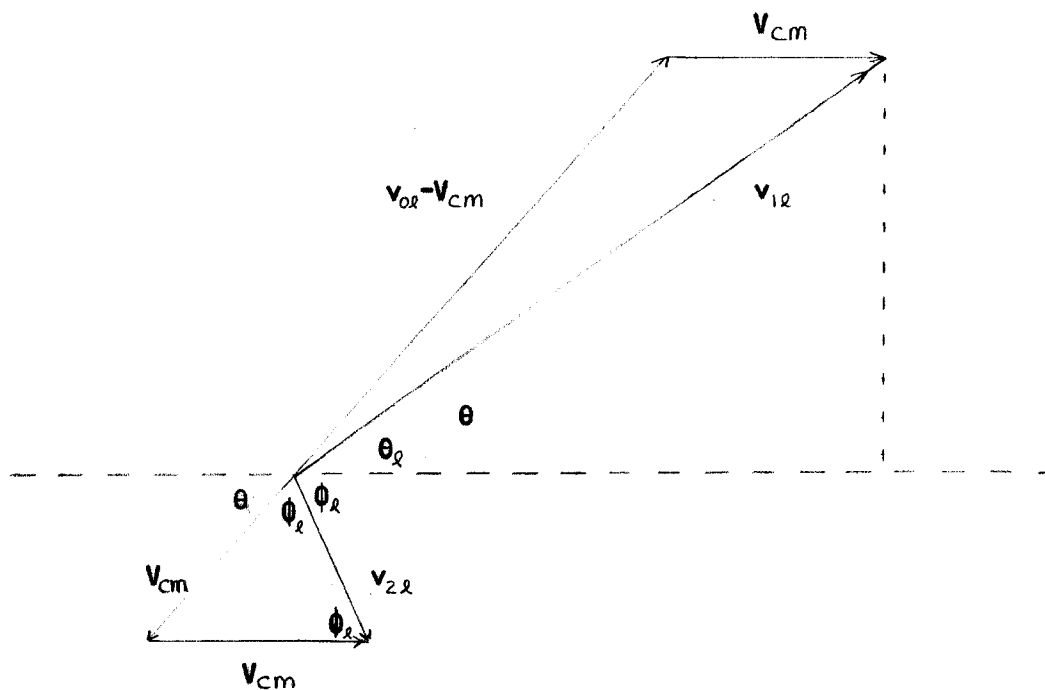


Fig. 13. A vector addition diagram of the velocities of the particles in the CM and lab frames.

$$\tan \theta_l = \frac{(v_{0l} - v_{cm}) \sin \theta}{v_{cm} + (v_{0l} - v_{cm}) \cos \theta} = \frac{\sin \theta}{m_1/m_2 + \cos \theta}$$

The second step follows by the definition of the center of mass velocity:

$m_2 v_{cm} = m_1 (v_{0l} - v_{cm})$. Note that if $m_1 \ll m_2$, $\theta \simeq \theta_l$ and the lab and CM

systems are almost identical. For the case $\theta_l = \theta_L = 136.4^\circ$, the CM

scattering angles are 136.6° , 137.2° , 137.8° , and 138.6° for ^1H , ^4He , ^7Li and ^{11}B respectively, if $m_2=197$.

Also from Fig. 13 we see that

$$v_{2\ell} = 2 v_{cm} \sin(\pi/2 - \phi_{\ell})$$

and
$$2 \phi_{\ell} = \pi - \theta.$$

Hence
$$v_{2\ell} = 2 v_{cm} \sin(\theta/2)$$

and the kinetic energy transferred to the target if the incident projectile is elastically scattered through θ is

$$T_{\ell} = \frac{1}{2} m_2 v_{2\ell}^2 = \frac{4m_1 m_2}{(m_1 + m_2)^2} E \sin^2(\theta/2). \quad (27)$$

III:1 Relationship of the Cross Sections

In an actual experiment the counting rate of a fixed detector is independent of the reference frame of the observer,

i.e.
$$\left(\frac{d\sigma}{d\Omega}\right) d\Omega = \left(\frac{d\sigma}{d\Omega}\right)_{\ell} d\Omega_{\ell}$$

For scattering by spherically symmetric potentials, the scattering distribution is independent of the azimuthal angle, so that

$$\frac{d\Omega_{\ell}}{d\Omega} = \frac{\sin \theta_{\ell} d\theta_{\ell}}{\sin \theta d\theta}.$$

Substituting in $\theta_{\ell} = \theta_L = 136.4^{\circ}$ and the CM scattering angles determined above, the ratios $(d\Omega_{\ell}/d\Omega)$ for ^1H , ^4He , ^7Li and ^{11}B on Au are found to be 1.0074, 1.0302, 1.0538 and 1.0956 respectively. The cross sections calculated in the CM system are converted to the lab system by dividing by these factors.

APPENDIX IV

EXPERIMENTAL DIFFERENTIAL SCATTERING CROSS SECTION

Consider a thin target film of thickness t and density N atoms per unit volume. In a thin film no target atom is blocked by any other. Suppose a collimated beam of monoenergetic projectiles and cross-sectional area A strikes the film at normal incidence. The number of scattering centers in the path of the beam is given by the product AtN . Denoting the differential cross section per target atom for scattering into a unit solid angle in the direction θ_ℓ in the laboratory system by $\frac{d\sigma(\theta_\ell, E_\ell)}{d\Omega}$, the effective target area presented to the beam for such scattering is

$$AtN \frac{d\sigma(\theta_\ell, E_\ell)}{d\Omega}$$

where E_ℓ is the lab energy. The fraction of the incident particles backscattered into the unit solid angle is

$$Nt \frac{d\sigma(\theta_\ell, E_\ell)}{d\Omega}$$

If a detector subtends a lab solid angle $\Delta\Omega$, and the fraction of the incident ions detected is denoted by B (the backscatter yield), then

$$B \approx Nt \frac{d\sigma(\theta_\ell, E_\ell)}{d\Omega} \Delta\Omega .$$

The lab differential scattering cross section is then

$$\frac{d\sigma(\theta_\ell, E_\ell)}{d\Omega} \approx \frac{B}{N(\Delta\Omega)t} . \quad (32)$$

BIBLIOGRAPHY

- Abrahamson, A. A. 1963. Phys. Rev. 130, 693.
- Behrisch, R. 1968. Can. J. Phys. 46, 527.
- Behrisch, R. 1969. Phys. Letters, 30A, 506.
- Bergstrom, I. and Domeij, B. 1966. Nucl. Instr. Methods 43, 146.
- Bohr, N. 1948. kgl. Danske Videnskab. Selskab. Mat. Fys. Medd. 18, No. 8.
- Everhart, E., Stone, G. and Carbone, R. J. 1955. Phys. Rev. 99, 1287.
- Firsov, O. B. (1958). Soviet Phys. -JETP 7, 308.
- Goldstein, H. Classical Mechanics (Addison-Wesley Publ. Co., Inc., Reading, Mass, 1959), Chapter 3.
- Lindhard, J. and Scharff, M. 1961. Phys. Rev. 124, 128.
- Lindhard, J., Nielsen, V., Scharff, M. and Thomsen, P. V. 1963. kgl. Danske Videnskab. Selskab. Mat. Fys. Medd. 33, No. 10.
- Marton, J. P. and Schlesinger, M. 1969. J. Appl. Phys. 40, 4529.
- Mayer, J. W., Eriksson, L., Picraux, S. T. and Davies, J. A. 1968. Can. J. Phys. 46, 663.
- McCracken, G. M. and Freeman, N. J. 1969. Proc. Phys. Soc. B, 2, 661.
- Mott, N. F. and Massey, H. S. W. Theory of Atomic Collisions (Oxford University Press, London, 1965), p. 110.
- Sigmund, P. 1968. Can. J. Phys. 46, 731.
- Sigmund, P. 1969. Phys. Rev. 184, 383.
- Smith, F. T., Marchi, R. P., Aberth, W., Lorents, D. C., and Heinz, O. 1967. Phys. Rev. 161, 31.
- van Wijngaarden, A., Miremedi, B., Brimner, E. J. and Bradford, J. N. 1970. Can. J. Phys. (May Issue).
- Whaling, W. 1958. Handbuch der Physik (Springer-Verlag, Berlin), Vol. 34, p. 192.

VITA AUCTORIS

Born November 6, 1946 in Leamington, Ontario.

Received elementary and secondary school education at Harrow, Ontario.

Graduated from University of Windsor with B. Sc. in Physics in 1969.